FULL PAPER

Nanodiamond Biosensors

ADVANCED
OPTICAL
MATERIALS

www.advopticalmat.de

Propagation Loss-Immune Biocompatible Nanodiamond Refractive Index Sensors

Roman Shugayev* and Peter Bermel*

Propagation loss is a key impeding parameter affecting accuracy, range, and applicability of fluorescent microscopy techniques. In this work, a new nanophotonic platform for propagation loss mitigated fluorescent imaging using lifetime ratiometric measurement is proposed. By applying this methodology to local parameter sensing, a method for high sensitivity local refractive index measurement via lifetime/energy monitoring of fluorescent crystal color centers is numerically demonstrated. As the base of this platform, biocompatible diamond nanodisk structures are investigated that enable sensitive, propagation loss-immune monitoring of refractive index changes both in vitro and in vivo.

1. Introduction

In the rapidly growing field of biophotonic sensing, subtle optical refractive index changes can help pinpoint biological activity, level of protein production, cell structure, and disease, which is particularly relevant in the absence of other markers in cases like cancer.[1–3] In particular, the basic fundamental feature of metabolism of cancer cells, namely, increased protein production driven by an enlarged, frequently dividing nucleus, can have a clear optical signature: a distinctly greater refractive index (RI). For example, cancerous cells can have refractive indices from 1.392 to 1.401, which is significantly larger than the typical value for normal cells of 1.35–1.37;[4] similarly, rat kidney cells appear to have an increased RI associated with cancerous activity.[5]

Clearly, technologies capable of accurately capturing this biophotonic information quickly, accurately, and inexpensively could be of great value. As a result, there has recently been increasing interest in complementing established nonoptical approaches such as X-rays, computerized axial tomography, and magnetic resonance imaging (MRI) with optical techniques for high-resolution diagnostics.[6,7] Methods such as full-field optical coherence microscopy,[8] autofluorescence,[9] and probe-based fluorescence,[10] diffused imaging and photoacoustic approaches[11] have all found various applications in cancer detection. Optical techniques have recently been applied to study cancers of the lung, breast, skin, esophagus, bladder,

colon, and more.[12] More specifically, optical techniques based on sensing refractive index changes induced by increased metabolic activity can be particularly advantageous for early diagnosis of rapidly progressing testicular, pediatric, and mesenchymal cancers, characterized by short tumor volume doubling times.[13]

Nonetheless, several challenges remain in current optical cancer diagnostics, which can be divided into two categories. Noninvasive microscopy approaches often have limited RI resolution, which means errors are often comparable to differential signals, limiting accuracy.[5] In probe-based (invasive) techniques, optical probes can be selectively concentrated in tumorous tissue via increased tumor vascularization and leaky blood vessels; still, refractive index errors can be significant, because of background scattering and extinction.[14] This issue becomes much more significant for nonepithelial deep tissue imaging. Furthermore, many of these materials, such as plasmonic metals like silver and its oxides, can present long-term toxicity hazards.[15,16] This effect is exacerbated by immune system uptake through phagocytosis.[17] Hence, devising a system to accurately detect local optical refractive index in a minimally invasive fashion with increased depth of penetration has presented a major challenge.

Recently, fluorescence lifetime imaging has received an increasing amount of interest as a tumor imaging technique.[18–20] In this paper, we propose a new modality for fluorescent sensing—propagation loss-immune monitoring of local refractive index using the ratio of optical signals originating from the same sensor having the same wavelength and polarization and differing by their energy and lifetime, defined here as lifetime ratiometric measurement. Breaking traditional nanoparticle spherical symmetry and employing the lifetime ratiometric measurement, we numerically demonstrate a new sensitive self-calibrated technique for fluorescent emission measurement at nanoscale.

Propagation through turbid media has been a long-lasting challenge for researchers in various fields of biological science, astronomy and atmospheric science, plasma diagnostics, and others. With the advent of adaptive optics wavefront aberrations could be effectively corrected and the information restored.[21] Alternative techniques such as speckle imaging, lucky imaging, and others have greatly improved image quality, however, they could not fully address fundamental issue of lost and corrupted information on the random path due to varying absorption, scattering, anisotropy, etc. Fortunately, with emergence of nanotechnology, advanced materials enabling new approaches to sensing and bioimaging have become available.

Dr. R. Shugayev, Prof. P. Bermel
School of Electrical and Computer Engineering
Birck Nanotechnology Center
Purdue University
1205 West State St., West Lafayette, IN 47907, USA
E-mail: rshugaye@purdue.edu; pbermel@purdue.edu

The ORCID identification number(s) for the author(s) of this article can be found under https://doi.org/10.1002/adom.201700487.

One of the most promising new materials is diamond.[22] Indeed, it has high biocompatibility and survivability, allowing for continuous particle tracking in live cells over periods up to multiple weeks. Diamond offers a large variety of color centers with long fluorescent lifetimes that can effectively eliminate autofluorescent background in delayed fluorescent measurement.[22–24] Nanodiamonds have good uptake by the cells, with endocytosis being particularly efficient in cancer cells.[25] As a result, nanodiamond particles recently have found increasing use in fluorescent probe imaging, local magnetic field, and temperature sensing.[22–24] In our work, we employ polarized emission property of diamond vacancy centers which arises from its crystalline structure.

2. Theory and Methods

A number of diamond color centers have been investigated over the years as promising candidates for quantum computing and sensing. These color centers include nitrogen vacancy (NV) centers, silicon (Si), xenon (Xe), nickel (Ni), and others. In this work, we primarily consider Xenon color centers due to the fact that both absorption (λ_{abs} = 647 nm) and emission (λ_{em} = 794 nm) are located within the biological transparency window and polarized.[26] The Xenon color center in diamond is a divacancy center[27] with trigonal symmetry (**Figure 1**), having emission dipole moments oriented along the main diagonal of the unit cell, as well as other symmetric directions.[28] Furthermore, xenon color center excitations are long-lived, aiding in time-dependent detection. Additionally, Xenon defect creation in diamond using ion implantation results in fairly high conversion efficiencies, which can reach up to 30% at room temperature.

Creating diamond nanoparticle doped with the described vacancies has been utilized for several fluorescent techniques.[23,24] For our purpose of distinguishing between polarized emissions for ratiometric measurement, we must break the crystalline symmetry of the nanoparticle. Additionally the resulting structure must possess high sensitivity to the parameter to be measured—local refractive index.

Normally, for continuous media, the electric dipole (ED) spontaneous emission rate is directly proportional to the RI.

Confinement of the dipole and consideration for local fields can significantly alter this simple dependence.[29] It has been shown analytically that emission rate for electric dipoles polarized out of plane in optically thin sheets scale as n^4, relative to the emission of transverse dipoles.[30] At the same time, scaling of the transverse dipole is proportional to medium refractive index, hence total scaling of the orthogonally polarized dipole is n^5 for an infinite sheet. Therefore, we can define a basic sensitive structure with a broken symmetry—diamond nanodisk geometry, whose properties in the limit of infinite radius approach those of the thin sheet (Figure 1a), e. g., for a 100 nm diameter disk, the sensitivity was found to be $n^{4.75}$, as is shown in **Figure 2**.

Orientations of dipole emitters in this structure would be set by the crystalline symmetry; p_z dipoles oriented along the [111] crystal direction will produce emission highly sensitive to RI, much like a 2D sheet. Laterally oriented electric dipoles (p_x, p_y) will have higher emission rates and can be separated from other polarizations within a single time-resolved fluorescent measurement.

Using the ratio of the orthogonal to transverse dipole emission in the resulting structure effectively cancels propagation loss effects and permits extraction of the local environment based parameters. In contrast with traditional ratiometric techniques such as fluorescence resonance energy transfer (FRET) that employ the ratios of the signals at different wavelengths,[31] here, calibration of our lifetime radiometric measurement is performed using signals at the same wavelength. Additionally, to ensure maximum cancelation of both slow varying and fast varying signals, propagating signals must have the same polarization and therefore experience same absorption and scattering loss. This is achieved via addition of the polarizer to the optical measurement setup. While dipole moments are orthogonal the dot product of resulting electric fields is, in general, nonzero. Indeed, for dipole radiation the field propagating into the far field is given by[32]

$$\mathbf{E} = \frac{1}{4\pi\varepsilon_0}\left[k^2(\mathbf{n}\times\mathbf{p})\times\mathbf{n}\right]\frac{e^{ikr}}{r} \tag{1}$$

where **p** is electric dipole moment, **n** and r are unit vector and distance to the observation point, and ε_0 is a permittivity of free space the dot product becomes
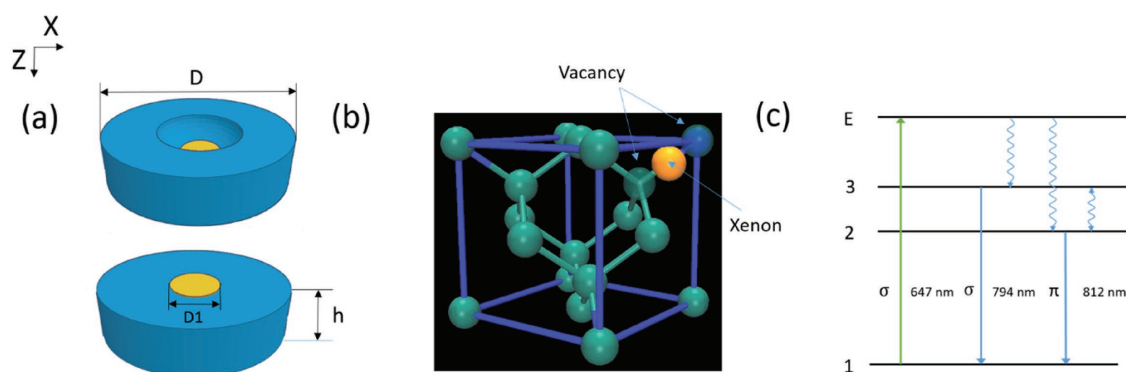

Figure 1. Nanodisk diamond structures for refractive index sensing. Nanodisk Z axis corresponds to [111] diamond crystalline direction. a) Dented (top) and unmodified (bottom) diamond disk structures; xenon-implanted regions are shown in yellow. b) Xenon color center location within the diamond crystal, which includes two adjacent vacancies. c) Energy diagram of the Xenon center.[26] Straight lines indicate optical transitions. Wiggly lines show nonradiative transitions.
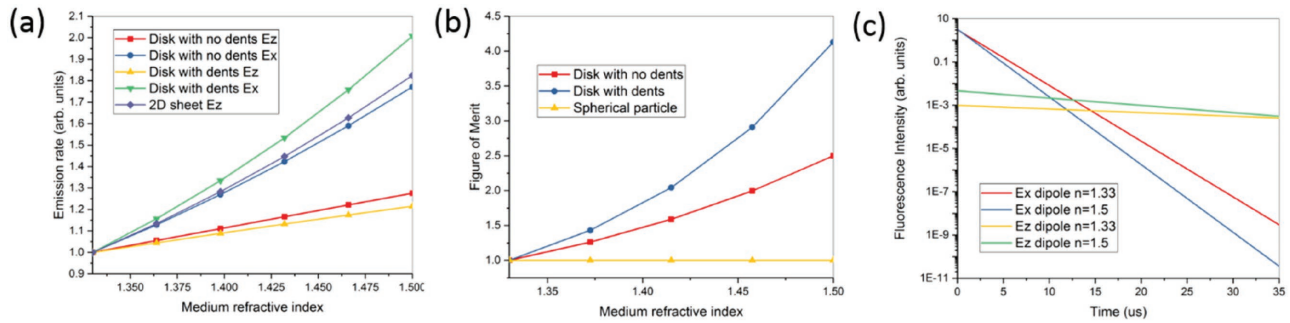
Figure 2. a) Emission rate versus the local medium refractive index for nanodisk structures and b) the figure of merit as defined in Equation (3) for nanodisk structures versus the local medium RI. Note that the absolute emission rates and FOM ratios are scaled to show the relative change. c) Average fluorescence intensity generated by the dented disk versus time.

$$\mathbf{E}_z \cdot (\mathbf{E}_x + \mathbf{E}_y) = \frac{k^4}{(4\pi\varepsilon_0)^2}(\mathbf{n} \cdot \mathbf{p}_z)((\mathbf{n} \cdot \mathbf{p}_x) + (\mathbf{n} \cdot \mathbf{p}_y))\frac{e^{i2kr}}{r^2} \tag{2}$$

which reduces to zero only when $\mathbf{n} = \hat{\mathbf{z}}$, and $\mathbf{n} \cdot \hat{\mathbf{z}} = 0$. Additionally, by considering $\mathbf{E} \times \mathbf{H}$ product, it can be shown that circulating and propagating power are decoupled in all emission field regions ensuring the same degree of attenuation for both $\mathbf{p}_x$ and $\mathbf{p}_y$ originated fields.

To quantify the change in refractive index of the local medium n, we, therefore, can define ratiometric figure of merit

$$F(n) = \frac{1}{N}\sum_i^N \frac{\Gamma_i^z(n)}{\Gamma_i^{x,y}(n)} \cdot \frac{E_i^z(n)}{E_i^{x,y}(n)} \tag{3}$$

where $\Gamma_i^z(n)$, $\Gamma_i^{x,y}(n)$, and $E_i^z(n)$, $E_i^{x,y}(n)$ are electric dipole emission rates and corresponding detected energies obtained from the time resolved measurement. Allowed $E_i^{x,y}(n)$ values must be limited to prevent excitations perpendicular to the nanodisk plane from creating unreasonably large ratios, by omitting probes with $E_i^{x,y}(n) < \delta E_{max}^{x,y}(n)$ in a given tissue region, where δ is a threshold defined by experiment. In the suggested figure of merit we also balanced the variation of the lifetime due to superradiant effects.[33]

We can further investigate the detected energy term. At room temperature, there are two radiative processes determining the emission of the Xenon color center—electric dipole $(\sigma - \sigma)$ and magnetic dipole $(\sigma - \pi)$ transitions (Figure 1c), with the ratio given by $\Gamma^{MD}(n)/\Gamma(n) = 5$ for bulk diamond.[26] As these are competing processes the detected energy emitted through ED transition is as follows

$$E(n) = \varepsilon(n)\frac{\Gamma(n)}{\Gamma(n) + \Gamma^{MD}(n)}e^{-\alpha r} \tag{4}$$

where $\varepsilon(n)$ is absorbed energy and magnetic dipole emission rate $\Gamma^{MD}(n) \propto n^3$. Using Beer's law all signal propagation losses are lumped into a single exponential factor.

Combining Equations (3) and (4) expression for effective figure of merit becomes

$$F(n) = \frac{1}{N}\sum_i^N \left(\frac{\Gamma_i^z(n)}{\Gamma_i^{x,y}(n)}\right)^2 \cdot \frac{\varepsilon_i^z(n)}{\varepsilon_i^{x,y}(n)} \cdot \frac{(\Gamma_i^{x,y}(n) + \Gamma_i^{MD}(n))}{(\Gamma_i^z(n) + \Gamma_i^{MD}(n))} \tag{5}$$

with the loss factors effectively canceling in the ratio.

Using the simulated data and averaging over all angles we obtained the dependence of the figure of merit on refractive index scales as $n^{8.6}$ for a simple disk structure.

Additional improvement in refractive index sensitivity of the basic structure can be achieved by phenomenological analysis of the sensitivity in the vicinity of the dipole embedded in the dielectric disk. Disk structure suppresses the emission by forcing the majority of emitted energy from $\hat{\mathbf{z}}$ dipole to reflect and be absorbed by the dipole. This mechanism is highly sensitive to the refractive index contrast between medium and the disk. It is possible to increase refractive index sensitivity by enhancing the efficiency of this process. The near field dipole emission pattern has the following electric field distribution

$$\mathbf{E} = \frac{1}{4\pi\varepsilon_0}\left[3\mathbf{n}(\mathbf{n} \cdot \mathbf{p}) - \mathbf{p}\right]\frac{1}{r^3} \tag{6}$$

which is composed of the terms propagating into the far-field and circulating power terms. It can be seen that the electric field component $\mathbf{E}\|\mathbf{p}$ has a sign change when $|\mathbf{p}| = 3(\mathbf{n} \cdot \mathbf{p})$ indicating the field minimum. We can introduce a taper that focuses the back reflected energy to the dipole location while providing minimal perturbation of the dipole radiation pattern by following the zero-field contour. Using this notion, we add spherical indentations approximating field lines on top and the bottom surface (Figure 1a). The shapes of indentations were chosen to facilitate fabrication of the structure. Indeed, this combined design increases the RI sensitivity of E_z dipoles from $n^{4.75}$ to $n^{5.8}$ (Figure 2a). Additionally, the taper also reduces the sensitivity of transverse dipole due to reduction of the effective thin layer thickness in the dipole vicinity. The corresponding figure of merit on refractive index scales as $n^{12.7}$ for a dented disk structure which would result in 39% contrast between healthy and cancerous tissue described in Ref. [4].

3. Results

Across the physiologically relevant optical refractive index range from 1.33 to 1.5, the figure of merit combing emission rate and energy flux measurement for dented and undented disks is 313% and 150%, respectively (Figure 2b). This greatly exceeds what could be seen using conventional geometries, as was confirmed by our simulations. The doped region can be

ADVANCED
SCIENCE NEWS
www.advancedsciencenews.com

ADVANCED
OPTICAL
MATERIALS
www.advopticalmat.de

approximated as a distributed source, which after averaging over the large number of doped emitters effectively cancels the propagation losses. Alternatively, cancelation can be achieved using a single vacancy emitter containing orthogonal dipole moments in the same optical transition line, as in the case of a diamond NV center, with a $E_x, E_y \rightarrow {}^3A_2$ zero phonon line transition.[34]

The changes in optical response with refractive index from our approach are strongly nonlinear, yet smooth enough to permit interpolation and differentiation of areas with small refractive index differences. Competing MD and ED dipole emission results in 84% enhancement in figure of merit range (dented disk) which is due to $\Gamma_i^z(n) \ll \Gamma_i^{MD}(n)$ from high suppression of orthogonal dipole emission. In general, the mechanism for enhancing figure of merit through competing processes is not limited to radiative transition but can also be employed using nonradiative processes that satisfy $\Gamma_i^z(n) \ll \Gamma_i^{NR}(n)$. Proposed mechanism for lifetime ratiometric sensing is highly generic and can be applied to wide range of established and emerging fluorescent sensing modalities. Utilizing this technique for par-

ticle tracking, drug delivery, magnetometry, and FRET-based approaches, significant improvements in the limit of detection and signal to noise ratios are expected.

4. Discussion

To design an effective RI sensing structure, we built on prior work demonstrating 100 nm diameter nanodiamond spheres used for cell tracking.[14] Thus, we started our simulations by selecting a nanodisk particle with $d = 100$ nm and $h = 20$ nm (Figure 1a). In this case, the sensitivity to refractive index change is only marginally less than that of an infinite 2D sheet (Figure 2a). Parameter optimization suggests that the radius of curvature for the spherical indentation for this structure should be $r = 15$ nm with 5 nm minimum distance between upper and lower surfaces. The location of the color centers is restricted to a uniformly doped central region with $D_1 = 10$ nm (Figure 1a, highlighted area). Additionally, local field effects were accounted for, following previous work.[35] Simulations were performed with finite-difference
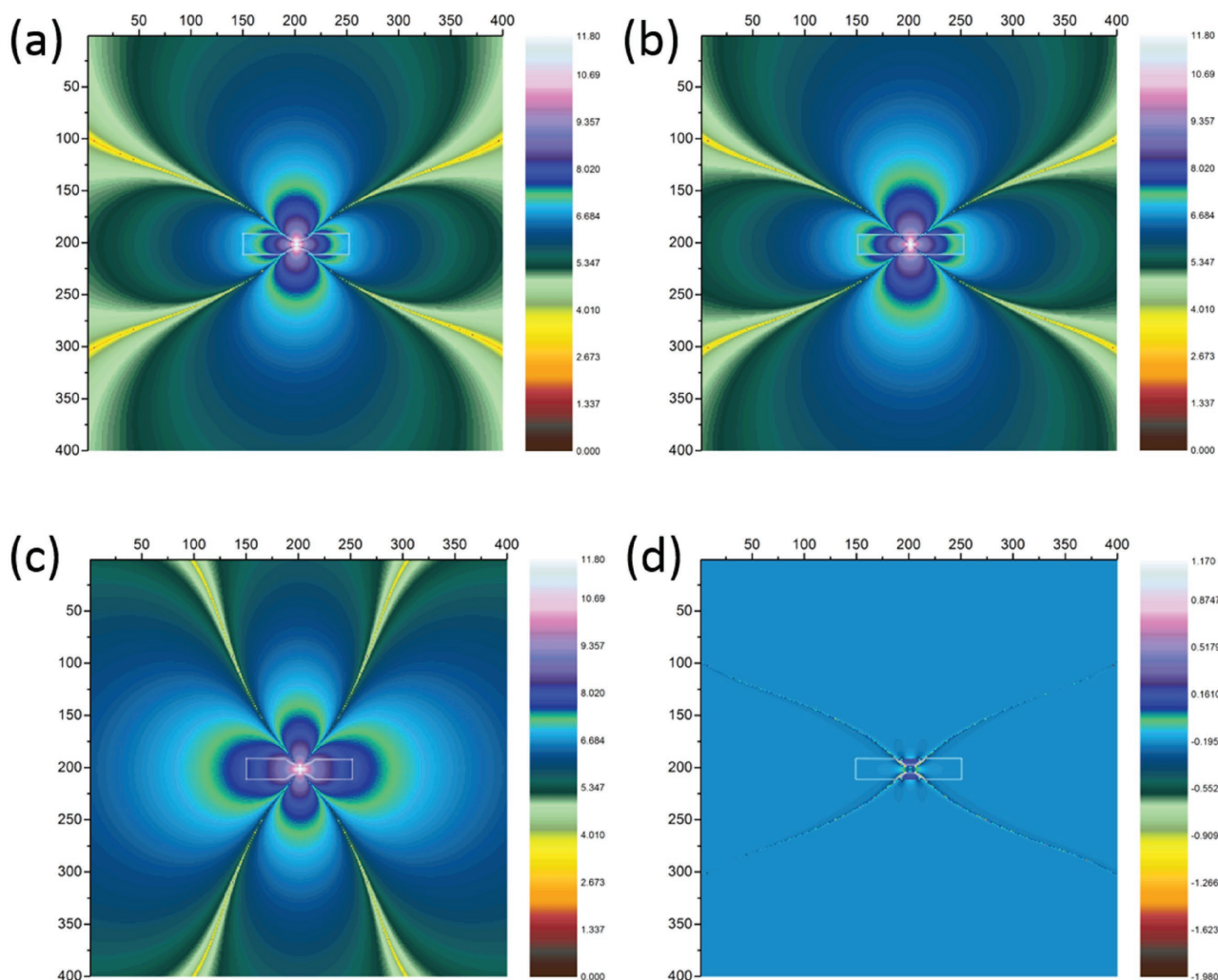

Figure 3. Snapshot of the logarithm of magnitude of electric field components during emission with dielectric structure traced as a contour: a) E_z with dents for an out-of-plane dipole; b) E_z without dents for an out-of-plane dipole; c) E_x with dents for an in-plane dipole; d) logarithm of the ratio of the electric fields depicted in (b) and (a). Spatial dimensions are given in nanometers.

**ADVANCED
SCIENCE NEWS**

www.advancedsciencenews.com

**ADVANCED
OPTICAL
MATERIALS**

www.advopticalmat.de

time-domain method using a freely available software package, known as MEEP.[36] The refractive index of the diamond was assumed to be 2.4, while the local medium index was varied from 1.33 to 1.5. All media were assumed to be lossless. A high-speed laser pulse provided the initial excitation, and emission was normalized to the baseline case of $\tau_0 \approx 1$ µs lifetime in diamond. Emission was obtained by integrating emitted power over the flux planes surrounding the emission volume of the structure. Absorption was simulated assuming an incident plane wave with $\lambda_{abs} = 647$ nm normalized to the same incident power.

We can also consider the dynamics of the fluorescence (Figure 2c). In the earlier research, multiplexed probes with small fluorescence lifetime difference have been successfully resolved in time-resolved fluorescent imaging.[37] Significant

mismatch of emission and absorption rates in the case of nanodisk fluorescence would facilitate separation of the fast and slow dipole signals in time domain. Shift in fluorescence intensity from the fast dipole-dominated to slow dipole-dominated can also be observed at ≈12.5 µs.

Due to the deeply subwavelength dimensions of the structure, the far-field emission pattern remains that of an electric dipole (Figure 4c,d), indicating that the propagating fields are not perturbed by the addition of this thin layer. The power guiding effects from the indentation can be observed in the immediate vicinity of the dipole (**Figure 3**a,b,d). The thin layer does not support propagating modes due to k-vector mismatch at the boundaries. The observed sharp contrast in the net propagating power perpendicular to the dipole (**Figure 4**a)
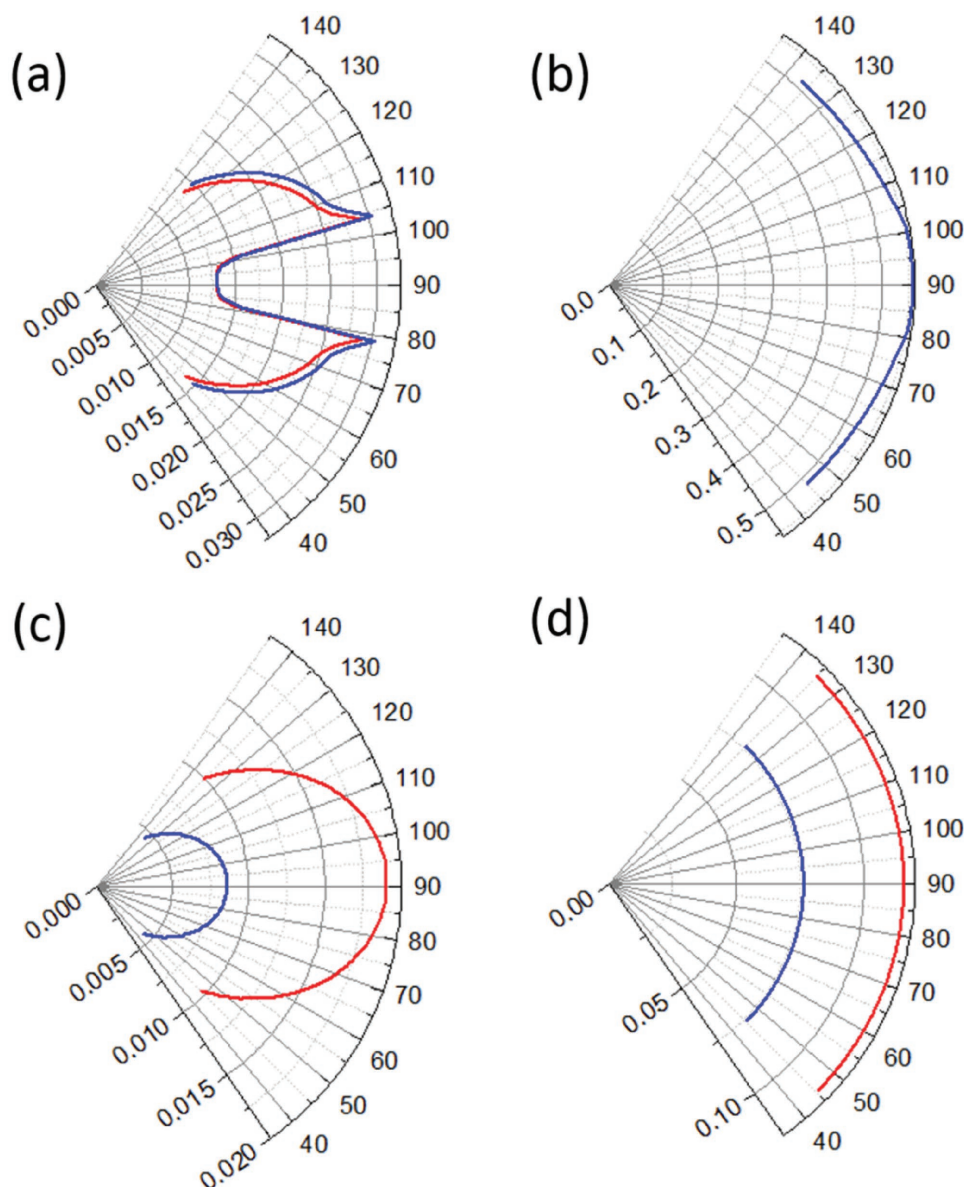

Figure 4. Power fluxes through the Y plane (90° corresponds to Y axis) at y = 50 nm for dipoles a) out-of-plane (E_z) and b) in-plane (E_x); as well as at y = 150 nm for dipoles c) out-of-plane (E_z) and d) in-plane (E_x). Blue lines corresponds to dented disk, red lines to disk with no dents. (a) and (b) graphs have been normalized to the same value at $\theta = 90°$. Centrally positioned dipole sources are assumed.

**ADVANCED
SCIENCE NEWS**

www.advancedsciencenews.com

**ADVANCED
OPTICAL
MATERIALS**

www.advopticalmat.de

is due to circulating energy being efficiently emitted, despite of the presence of the thin layer. Additionally, as a result of the increased coupling efficiency to and from the thin layer for a dented structure, the suppression of emission is further increased (Figure 4c).

In this paper, we have analyzed emission from Xenon color centers having a relatively long base lifetime; however, the range of available impurities in diamond makes it possible to tailor the emission spectrum for specific applications. Since the lifetimes of the emitters in the diamond can span 2–3 orders of magnitude, it would be feasible to optimize such tradeoffs as implantation dose/spot size, propagation loss cancelation and probe brightness. Additionally for generic implementation of lifetime ratiometric method other host crystalline materials with defined orientations of impurity centers should also be considered.

Fabrication of the proposed nanodisk structures can be achieved using thin layer deposition techniques[38] as well as recently proposed methods for diamond conversion from the stacked graphene sheets.[39] Focused ion beam implantation, reactive ion etching, and masked processing can be used as processing steps.[40–42]

Going forward, there may be interest in adopting these nanodisks for clinical applications. A number of inorganic particles targeted for use in diagnosis and therapy have shown success in preclinical trials, and are currently undergoing various stages of approval for clinical use.[43–45] Along similar lines, translation of the proposed local refractive index sensor into the clinic will need to take place in stages. First, the expected functionality must be confirmed in the laboratory, using controlled refractive index environment tests.[46] Second, in vitro tests of nanodisk cellular uptake, as well as comparative healthy/malignant tissue analysis must take place. Third, in vivo animal studies should follow, with confirmation of function through biodistribution, assessed using dissections.[47] Finally, tests of the fate and usefulness of the nanoparticles in small animals and human subjects should be facilitated by utilizing radionuclide-labeled diamond nanodisks.[48,49]

5. Conclusion

Our proposed methodology offers a new paradigm for nanoscale sensing, via combining nanoparticle symmetry breaking with polarization property of nanodiamond emitters. The resulting ability to cancel propagation losses will improve performance and applicability of a wide range of fluorescence-based sensing and microscopy techniques. Aided by the biocompatibility and stability of the nanodiamond platform, these proposed devices can provide a minimally invasive way to track refractive index changes over extended time periods at the nanoscale, both in vitro and in vivo, compared to prior work. The high sensitivity of diamond nanodisk structures opens a pathway to multiple applications in biophotonic sensing and disease diagnostics, particularly high-resolution detection of cancer in proximity to healthy tissue.

Conflict of Interest

The authors declare no conflict of interest.

[1] A. C. Curry, M. Crow, *J. Biomed. Opt.* **2008**, *13*, 014022.
[2] P. Y. Liu, L. K. Chin, W. Ser, H. F. Chen, C. M. Hsieh, C. H. Lee, K. B. Sung, T. C. Ayi, P. H. Yap, B. Liedberg, K. Wang, *Lab Chip* **2016**, *16*, 634.
[3] Z. Wang, K. Tangella, A. Balla, G. Popescu, *J. Biomed. Opt.* **2011**, *16*, 116017.
[4] X. J. Liang, A. Q. Liu, C. S. Lim, T. C. Ayi, P. H. Yap, *Sens. Actuators A* **2007**, *133*, 349.
[5] W. J. Choi, D. I. Jeon, S. G. Ahn, J. H. Yoon, S. Kim, B. H. Lee, *Opt. Express* **2010**, *18*, 23285.
[6] M. Solomon, Y. Liu, M. Y. Berezin, S. Achilefu, *Med. Princ. Pract.* **2011**, *20*, 397.
[7] E. L. Kaijzel, G. van Der Pluijm, C. W. Löwik, *Clin. Cancer Res.* **2007**, *13*, 3490.
[8] W. J. Choi, D. I. Jeon, S. G. Ahn, J. H. Yoon, S. Kim, B. H. Lee, *Opt. Express* **2010**, *18*, 23285.
[9] M. Monici, *Biotechnol. Annu. Rev.* **2005**, *11*, 227.
[10] Y. Urano, D. Asanuma, Y. Hama, Y. Koyama, T. Barrett, M. Kamiya, T. Nagano, T. Watanabe, A. Hasegawa, P. L. Choyke, H. Kobayashi, *Nat. Med.* **2009**, *15*, 104.
[11] S. Mallidi, T. Larson, J. Tam, P. P. Joshi, A. Karpiouk, K. Sokolov, S. Emelianov, *Nano Lett.* **2009**, *9*, 2825.
[12] N. Bedard, M. Pierce, A. El-Naggar, S. Anandasabapathy, A. Gillenwater, R. Richards-Kortum, *Technol. Cancer Res. Treat.* **2010**, *9*, 211.
[13] S. Friberg, S. Mattson, *J. Surg. Oncol.* **1997**, *65*, 284.
[14] J. N. Anker, W. P. Hall, O. Lyandres, N. C. Shah, J. Zhao, R. P. van Duyne, *Nat. Mater.* **2008**, *7*, 442.
[15] M. Yamada, M. Foote, T. W. Prow, *Wiley Interdiscip. Rev.: Nanomed. Nanobiotechnol.* **2015**, *7*, 428.
[16] H. Bahadar, F. Maqbool, K. Niaz, M. Abdollahi, *Iran. Biomed. J.* **2015**, *20*, 1.
[17] S. Chapman, M. Dobrovolskaia, K. Farahani, A. Goodwin, A. Joshi, H. Lee, T. Meade, M. Pomper, K. Ptak, J. Rao, R. Singh, *Nano Today* **2013**, *8*, 454.
[18] M. Y. Berezin, S. Achilefu, *Chem. Rev.* **2010**, *110*, 2641.
[19] S. Bloch, F. Lesage, L. McIntosh, A. Gandjbakhche, K. Liang, S. Achilefu, *J. Biomed. Opt.* **2005**, *10*, 054003.
[20] R. E. Nothdurft, S. V. Patwardhan, W. Akers, Y. Ye, S. Achilefu, J. P. Culver, *J. Biomed. Opt.* **2009**, *14*, 024004.
[21] M. J. Booth, *Light: Sci. Appl.* **2014**, *3*, 165.
[22] Y. Zhu, J. Li, W. Li, Y. Zhang, X. Yang, N. Chen, Y. Sun, Y. Zhao, C. Fan, Q. Huang, *Theranostics* **2012**, *2*, 302.
[23] W. W. W. Hsiao, Y. Y. Hui, P. C. Tsai, H. C. Chang, *Acc. Chem. Res.* **2016**, *49*, 400.

[24] L. P. McGuinness, Y. Yan, A. Stacey, D. A. Simpson, L. T. Hall, D. Maclaurin, S. Prawer, P. Mulvaney, J. Wrachtrup, F. Caruso, R. E. Scholten, *Nat. Nanotechnol.* **2011**, *6*, 358.

[25] E. Perevedentseva, S. F. Hong, K. J. Huang, I. T. Chiang, C. Y. Lee, Y. T. Tseng, C. L. Cheng, *J. Nanopart. Res.* **2013**, *15*, 1834.

[26] A. A. Bergman, A. M. Zaitsev, A. A. Gorokhovsky, *J. Lumin.* **2007**, *125*, 92.

[27] A. B. Anderson, E. J. Grantscharova, J. C. Angus, *Phys. Rev. B* **1996**, *54*, 14341.

[28] A. A. Kaplyanskii, *J. Phys. Colloq.* **1967**, *28*, C4.

[29] P. Lavallard, *Acta Phys. Pol., Ser. A* **1996**, *90*, 645.

[30] W. Lukosz, *J. Opt. Soc. Am.* **1981**, *71*, 744.

[31] P. Lipp, E. Niggli, *Cell Calcium* **1993**, *14*, 359.

[32] J. D. Jackson, *Classical Electrodynamics*, Wiley, New York **1999**.

[33] R. H. Dicke, *Phys. Rev.* **1954**, *93*, 99.

[34] J. R. Maze, A. Gali, E. Togan, Y. Chu, A. Trifonov, E. Kaxiras, M. D. Lukin, *New J. Phys.* **2011**, *13*, 025025.

[35] G. L. J. A. Rikken, Y. A. R. R. Kessener, *Phys. Rev. Lett.* **1995**, *74*, 880.

[36] A. F. Oskooi, D. Roundy, M. Ibanescu, P. Bermel, J. D. Joannopoulos, S. G. Johnson, *Comput. Phys. Commun.* **2010**, *181*, 687.

[37] Y. Lu, J. Lu, J. Zhao, J. Cusido, F. M. Raymo, J. Yuan, S. Yang, R. C. Leif, Y. Huo, J. A. Piper, J. P. Robinson, *Nat. Commun.* **2014**, *5*, 3741.

[38] V. P. Popov, V. A. Antonov, L. N. Safronov, I. N. Kupriyanov, Y. N. Pal'yanov, S. Rubanov, in *AIP Conf. Proc.* (Eds: L. Pelaz, I. Santos, R. Duffy, F. Torregrosa, K. Bourdelle) **2012**, *1496*, 261.

[39] A. G. Kvashnin, L. A. Chernozatonskii, B. I. Yakobson, P. B. Sorokin, *Nano Lett.* **2014**, *14*, 676.

[40] C. S. Kim, S. H. Ahn, D. Y. Jang, *Vacuum* **2012**, *86*, 1014.

[41] H. Li, S. Cheng, J. Li, J. Song, *J. Nanomater.* **2015**, *2015*, 4.

[42] L. Li, I. Bayn, M. Lu, C. Y. Nam, T. Schröder, A. Stein, N. C. Harris, D. Englund, *Sci. Rep.* **2015**, *5*, 7802.

[43] A. C. Anselmo, S. Mitragotri, *AAPS J.* **2015**, *17*, 1041.

[44] D. Paithankar, B. H. Hwang, G. Munavalli, A. Kauvar, J. Lloyd, R. Blomgren, L. Faupel, T. Meyer, S. Mitragotri, *J. Controlled Release* **2015**, *206*, 30.

[45] E. Phillips, O. Penate-Medina, P. B. Zanzonico, R. D. Carvajal, P. Mohan, Y. Ye, J. Humm, M. Gönen, H. Kalaigian, H. Schöder, H. W. Strauss, *Sci. Transl. Med.* **2014**, *6*, 260ra149.

[46] W. Liang, Y. Huang, Y. Xu, R. K. Lee, A. Yariv, *Appl. Phys. Lett.* **2005**, *86*, 151122.

[47] Y. Yuan, Y. Chen, J. H. Liu, H. Wang, Y. Liu, *Diamond Relat. Mater.* **2009**, *18*, 95.

[48] H. A. Girard, A. El-Kharbachi, S. Garcia-Argote, T. Petit, P. Bergonzo, B. Rousseau, J. C. Arnault, *Chem. Commun.* **2014**, *50*, 2916.

[49] S. Rojas, J. D. Gispert, R. Martín, S. Abad, C. Menchon, D. Pareto, V. M. Víctor, M. Alvaro, H. García, J. R. Herance, *ACS Nano* **2011**, *5*, 5552